ADVANCED ELECTRONIC MATERIALS
www.advelectronicmat.de

Optimized Activation of Solution-Processed Amorphous Oxide Semiconductors for Flexible Transparent Conductive Electrodes

*Byung Doo Choi, Joohyung Park, Kang-Jun Baeg, Minji Kang, Jae Sang Heo, Seonhyoung Kim, Jongkook Won, Seungwoo Yu, Kyunghan Ahn, Tae Hoon Lee, Jongin Hong, Dong-Yu Kim, Hakan Usta, Choongik Kim, Sung Kyu Park, and Myung-Gil Kim**

Here, the preparation of transparent amorphous oxide semiconductor (AOS) films with unprecedented conductivity via an optimized activation process under hydrogen atmosphere for applications in solution-processed large-area optoelectronics is reported. Owing to their high cost and mechanical vulnerability, conventional vacuum-processed indium–tin oxide (ITO) electrodes are inappropriate for use in next-generation flexible and wearable electronic devices and systems. As an alternative to the ITO electrodes, solution-processed AOS films, such as *a*-IZO and *a*-ZITO, with an optimized composition and postreduction treatment under hydrogen show the highest electrical conductivity of ≈300 S cm^{-1} and a high optical transmittance of over 90% at 550 nm. The microstructures and electrical properties of these AOS films are also studied in order to determine the optimized chemical composition and postreduction conditions. It is found that a controlled hydrogen reduction treatment of AOS films is critical for achieving high electrical conductivity by suppressing the surface morphology degradation and grain boundary disconnection. Furthermore, the *a*-IZO transparent conductive electrodes are successfully implemented for high efficiency organic photovoltaic cells based on the PTB7/PC$_{71}$BM active layers. This technique promises the low-cost fabrication of high mobility and/or conductive AOSs for their applications in large-area transparent and flexible optoelectronics.

1. Introduction

Transparent conductive electrodes (TCEs) are widely used for various optoelectronic applications such as organic light-emitting diode (OLED), photovoltaic cells, and touch screens of high-end mobile devices.[1,2] There has been a long-term and intensive investigation of various TCE materials. Transparent conducting oxides (TCOs) exhibit excellent optoelectronic performances and have been industrially implemented for current large-area electronics. Indium–tin oxide (ITO) is a representative material that has been typically used as industrial TCEs. ITO electrodes are mostly fabricated with vacuum deposition techniques such as pulsed laser deposition, ion assisted deposition, and radio frequency (RF) magnetron sputtering.[3] In particular, the RF-sputtered indium–tin oxide (ITO) has been widely applied for front-planes of flat panel displays and current collecting layers of thin-film solar cells with high optical transparency

B. D. Choi, J. Park, S. Kim, J. Won, S. Yu, Dr. K. Ahn, Prof. J. Hong, Prof. M.-G. Kim
Department of Chemistry
Chung-Ang University
Seoul 06974, Republic of Korea
E-mail: myunggil@cau.ac.kr

Prof. K.-J. Baeg
Department of Graphic Arts Information Engineering
Pukyong National University
Busan 48547, Republic of Korea

Dr. M. Kang, Prof. D.-Y. Kim
Research Institute for Solar and Sustainable energies (RISE)
School of Materials Science and Engineering
Gwangju Institute of Science and Technology (GIST)
Gwangju 61005, Republic of Korea

J. S. Heo, Prof. S. K. Park
School of Electrical and Electronics Engineering
Chung-Ang University
Seoul 06974, Republic of Korea

Prof. T. H. Lee
Department of Electrical Engineering
Kwangwoon University
Seoul 01897, Republic of Korea

Prof. H. Usta
Department of Materials Science and Nanotechnology Engineering
Abdullah Gül University
Kayseri 38080, Turkey

Prof. C. Kim
Department of Chemical and Biomolecular Engineering
Sogang University
Seoul 04107, Republic of Korea

DOI: 10.1002/aelm.201700386

© 2017 WILEY-VCH Verlag GmbH & Co. KGaA, Weinheim

(≈89% at 550 nm wavelength) and excellent electrical conductivity (resistivity $\rho \leq 1 \times 10^{-4}\ \Omega$ cm).[4] However, with growing industrial demands, the relatively high cost and chemical instability of the ITO materials has resulted in significant research interest in developing alternative TCOs and processing techniques other than vacuum deposition.[5]

The newly developed TCO materials such as fluorine-doped tin oxide and aluminum-doped zinc oxide (ZnO:Al) are nontoxic, thermally stable, and inexpensive. They have been used for low-cost, large-area optoelectronic applications in OLEDs, thin-film and dye-sensitized solar cells, perovskites, and organic photovoltaics, and printed sensor arrays.[6] Unfortunately, these conventional vacuum-processed crystalline TCOs are inappropriate for next generation low-cost, printed and flexible optoelectronic devices, wearable devices, and biocompatible soft electronics.[7,8] Under continuous bending cycles, polycrystalline nature of the conventional TCO film inevitably resulted in mechanical failure at the grain boundary with significant degradation of electrical performance.[7] Moreover, the capital intensive vacuum equipment that is used for the conventional TCO fabrication technique of vacuum deposition is unsuitable for low-cost large-area electronic devices. In order to overcome these limitations of conventional TCOs, alternative TCE materials such as carbon nanotubes, conducting polymers (poly(3,4-ethylenedioxythiophene):polystyrene sulfonate, PEDOT:PSS), metal nanostructures (metal mesh or nanowires), and 2D materials (graphene, MoS_2, Bi_2Se_3) have been developed that display reasonable optoelectronic performances and superior mechanical stabilities compared to ITO.[9] Although the alternative TCE materials have been successfully demonstrated for next generation large area electronic applications, such as touch sensor, thin-film solar cell, and flexible display, there are partially resolved remaining issues such as the corrosive chemical nature, incompatibility with conventional electronic materials, poor scalability, and/or insufficient optoelectronic performance of TCE materials that need to be addressed before their commercial application.[10]

Amorphous TCOs have no grain boundary that is vulnerable to mechanical stress. Therefore, the many challenges faced with crystalline TCOs can be resolved by using these amorphous thin films, while still retaining their industrial compatibilities. The vacuum-deposited amorphous TCOs reportedly show mechanical stabilities that are ideal for flexible optoelectronic applications.[11] Moreover, similar superior mechanical stabilities have also been reported with the solution-processed amorphous oxide semiconductors (AOSs). The use of such AOSs can enable high throughput and low-cost fabrication processes, as well as facile chemical composition control with simple mixing of each precursor solution.[12,13] Despite the remarkable progress in the field of solution-processed AOSs and their applications in high-performance thin-film transistors (TFTs), only a few solution-processed amorphous TCOs have been investigated that exhibit inferior electrical conductivity (below 50 S cm^{-1}).[14–16] Unlike the semiconducting channel materials in TFTs, the highly conducting TCOs require large carrier concentration, which is typically generated from the corresponding large concentration of oxygen vacancies in AOSs.[13,15,17] While it is widely accepted that a highly oxidizing atmosphere is required to remove carbon impurities, the suppression of oxygen vacancy generation during oxidative annealing process can inversely hinder the effective activation of TCOs.

Herein we report the optimized activation of the solution-processed AOSs such as indium–zinc oxide (*a*-IZO), zinc–tin oxide (*a*-ZTO), and zinc–indium–tin oxide (*a*-ZITO). As a representative material, the chemical composition and activation conditions of *a*-IZO were studied in detail. Similar to a previous report on *a*-IZO TFT devices, the charge carrier mobility of *a*-IZO TCOs showed the highest optimized performance at In:Zn = 7:3. Although several crystalline TCO materials with higher electrical conductivities have been reported, they generally require very high temperatures for postreduction treatment (T_{red} > 500 °C) in order to generate a significant amount of oxygen vacancies and dopant activation. The *a*-IZO TCO developed in this work showed an optimized carrier activation with a low postreduction temperature of 250 °C under H_2 (5%)/Ar because of its enhanced carrier transport properties, which could be compatible with high temperature durable flexible plastic substrate, such as polyimide.[18] The optimized *a*-IZO-based TCEs exhibited high electrical conductivity of ≈300 S cm^{-1} with an electron mobility of 17.2 $cm^2\ V^{-1}\ s^{-1}$. With the optimized *a*-IZO TCE, we could successfully demonstrate organic photovoltaic cells based on the solution-processed amorphous TCO anodes.

2. Results and Discussions

The fabrication process of TCO films based on a solution-processed AOS is described in **Figure 1** and the preparation of metal oxide precursor solutions is described in the Experimental Section. The spin-coated soluble metal oxide precursors were initially annealed at high temperatures (450 or 500 °C) to ensure complete oxidation and carbon impurity removal. The solution-deposited AOS films were subsequently postreduced at different temperatures ranging from 150 to 450 °C under forming gas–base (5% H_2 and 95% Ar) conditions. The oxide semiconductor alloys with typical chemical compositions (ZnO, Ga_2O_3, SnO_2, In_2O_3, etc.) are known to have thermally stable amorphous phases.[16,19–21] Before fabricating the AOS films, we investigated common vacuum-deposited AOS-based TCOs such as *a*-IZO, *a*-ZTO, and *a*-ZITO.[16,19,22,23] In particular, *a*-IZO has been extensively used for the preparation of flexible amorphous TCOs.[16,19,22,23] The detailed investigations on *a*-IZO films such as electrical performance dependence on chemical compositions, optimized carrier activation conditions, and microstructural analysis, revealed that the postreduction conditions are the most important for fabricating high-performance AOS-based TCOs via solution process (similar to the results for *a*-ZTO and *a*-ZITO). Unlike the common approach that is used in solution-processed crystalline ITO to generate oxygen vacancies and subsequently achieve a high carrier concentration, the high temperature postreduction of AOS is not effective method to improve the electrical conductivity of solution-processed AOS-based TCOs.

The microstructural change within the *a*-IZO films can significantly affect the electron mobility and the corresponding electrical conductivity of the amorphous TCO films. **Figure 2**a

© 2017 WILEY-VCH Verlag GmbH & Co. KGaA, Weinheim

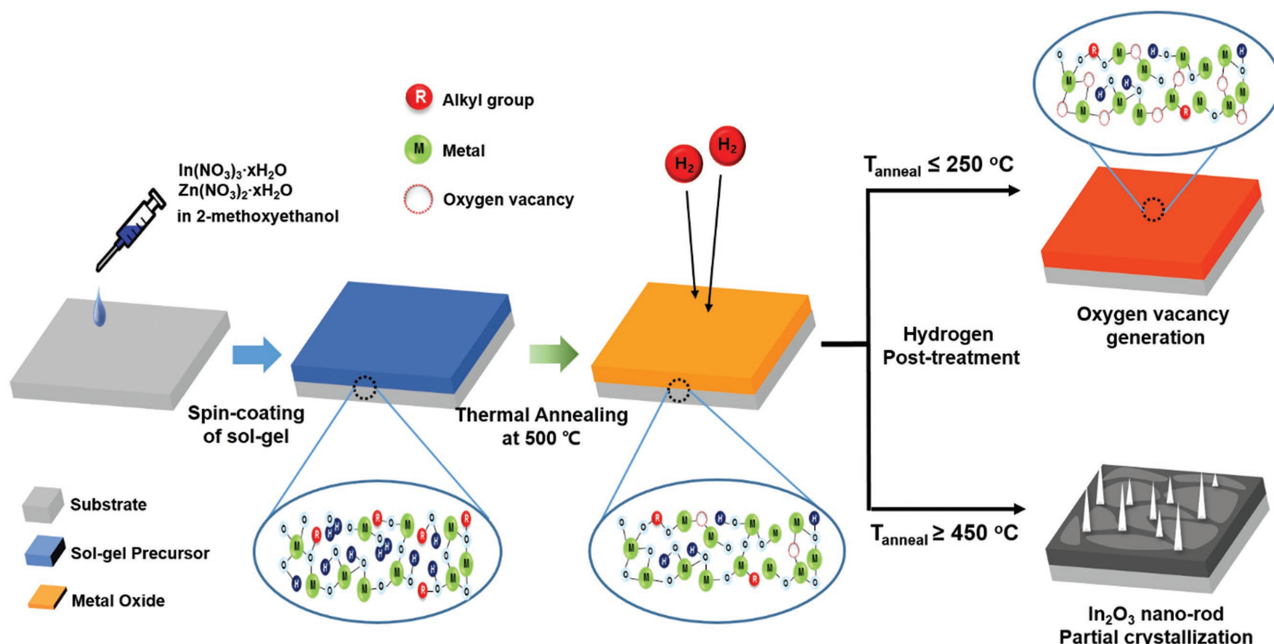

Figure 1. Schematic diagram of the solution processing of indium–zinc oxide transparent conductive electrode.

shows the grazing incidence angle X-ray diffraction (GIAXRD) patterns of the solution-processed $In_{11-2x}Zn_{2x-1}O_{15.5-x}$ (x = 1–5) films after thermal annealing at 500 °C in air. Under the Zn- or In-rich conditions of x = 1, 4, and 5, strong crystalline peaks of ZnO or In_2O_3 were observed. Notably, the GIAXRD patterns of $In_1Zn_9O_{10.5}$ and $In_3Zn_7O_{11.5}$ films showed clear crystalline peaks, which are consistent with the peaks observed from crystalline ZnO. Similarly, the GIAXRD pattern of the $In_9Zn_1O_{14.5}$ film matched well with the peaks of crystalline In_2O_3. On the other hand, the intermediate compositions such as $In_5Zn_5O_{12.5}$ and $In_7Zn_3O_{13.5}$ were revealed to have been formed as an amorphous phase, which is consistent with the broad GIAXRD peak around $2\theta = 30°–36°$.[16,24] The previous studies on *a*-IZO-based TFTs also showed a similar tendency of GIAXRD patterns and oxide lattice crystallizations with respect to the In to total metal molar ratio.[24–26] Moreover, the broad amorphous peaks for *a*-ZTO ($Zn_{0.3}Sn_{0.7}O_{1.7}$) and *a*-ZITO ($Zn_{0.7}In_{0.6}Sn_{0.7}O_{3.0}$) (shown as No reduction in Figure S1, Supporting Information) also confirmed the amorphous nature of the TCO films in this study. From the reported *a*-IZO TFT studies, it may be concluded that a high In content generally leads to higher electron mobility, which was also confirmed by the observation that the *a*-$In_7Zn_3O_{13.5}$ material synthesized under optimized conditions had the highest In content in the amorphous phase.

The thermal stability of amorphous oxide alloys under oxidative conditions such as O_2 and ambient air is well-known.[19–21] As shown in Figure 2b, we could also confirm the structural stabilities of amorphous $In_{11-2x}Zn_{2x-1}O_{15.5-x}$ (x = 3 and 4) up to 500 °C. However, the poor electrical performances of the solution-processed *a*-IZO after ambient air-annealing requires

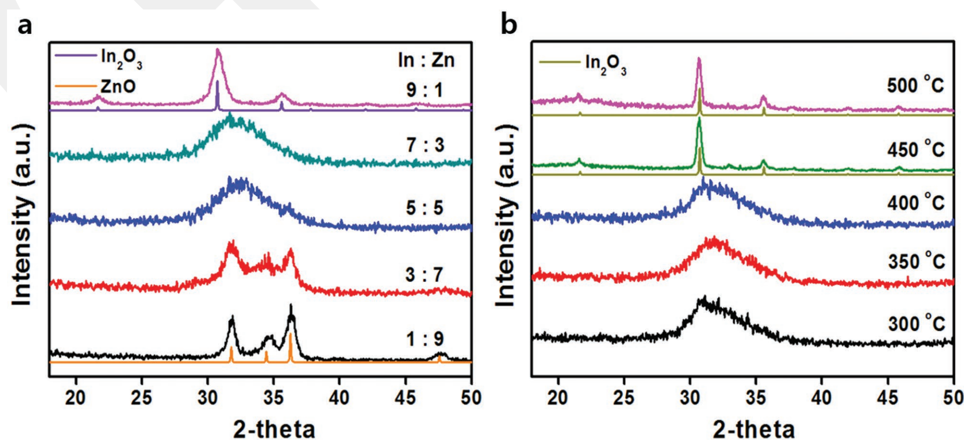

Figure 2. Grazing incident X-ray diffraction (GIXRD) of the IZO films. a) X-ray diffraction of the IZO films with respect to In:Zn ratio. b) X-ray diffraction of the optimized $In_7Zn_3O_{13.5}$ films dependent on H_2 reduction temperature.

© 2017 WILEY-VCH Verlag GmbH & Co. KGaA, Weinheim

a postreduction treatment in order to activate the amorphous TCOs with the generation of oxygen vacancies and subsequent increase in the free carrier concentration.[17] Although the reduction treatment of ITO was typically carried out to achieve a high carrier concentration, the chemical instability and facile crystallization of ITO under reduction conditions has been reported to occur at ≈250 and ≈370 °C with pure hydrogen and forming gas, respectively.[27] The uncontrolled over-reduction states resulted in decreased electrical performance of ITO after treating it at 350 °C with 8% forming gas.[27] Figure 2b shows the GIAXRD patterns of a-$In_7Zn_3O_{13.5}$ films after reduction treatment under 5% H_2/95% Ar with various temperature range from 300–500 °C. Unlike the oxidative air ambient treatment, the postannealing of AOS films in reducing environment could significantly increase the crystallization temperature. Therefore, our solution-processed a-$In_7Zn_3O_{13.5}$ films also showed distinctive crystallization peaks at ≥450 °C, which were coincident with those of crystalline In_2O_3; these observations are similar to those described in previous reports on the crystallization of ITO.[27] The crystalline phase formation of IZO films at high postreduction temperature of over 450 °C could be a critical factor for the deterioration of the electrical performance of the optimized amorphous IZO-based TCOs.

As observed in the atomic force microscopy (AFM) images in Figure S2 (Supporting Information) of as-deposited IZO films and those that were H_2-reduced at 250 °C, the optimized a-$In_7Zn_3O_{13.5}$ films exhibit a smoother surface morphology than the other IZO films with different In:Zn ratios. The root-mean-square (RMS) roughness of as-deposited and 250 °C H_2-reduced films is 0.594 and 0.539 nm, respectively (Table S1, Supporting Information). The AFM images of the $In_1Zn_9O_{10.5}$ and $In_3Zn_7O_{11.5}$ films given in Figure S2 of the Supporting Information show numerous grains and grain boundaries with high RMS roughness in the range of 3–8 nm, which reflects their strong crystalline nature, as confirmed with GIAXRD in Figure 2. Similarly, the rugged surface of Zn-rich films ($In_1Zn_9O_{10.5}$ and $In_3Zn_7O_{11.5}$) was also believed to be a result of the significant hygroscopic nature of the zinc nitrate-based precursor under ambient conditions, which resulted in poor surface uniformity during and/or after the spin-casting process.[15] With increase in the indium content up to $In_5Zn_5O_{12.5}$ and $In_7Zn_3O_{13.5}$, an extremely smooth surface morphology can be obtained with amorphous phases. Notably, a further increase of indium content up to $In_9Zn_1O_{14.5}$ again leads to a slightly higher RMS roughness (≈1 nm) because of the crystalline phase formation of the indium oxide structure.

The AFM images of a-$In_7Zn_3O_{13.5}$ films shown in **Figure 3** revealed that reducing temperatures above 300 °C can induce partial crystallization of the a-IZO films, which cannot be easily detected with the GIAXRD patterns given in Figure 2. Although the a-$In_7Zn_3O_{13.5}$ film H_2-reduced at 250 °C showed a flat surface without any noticeable grains (see Figure 3a), the IZO films of the same composition that reduced at a higher temperature started to grow crystalline grains with lateral sizes ranging from 132.5 nm and 294.5 to 372 nm for 300 °C and 350 to 400 °C, respectively. In contrast to the previously reported ITO films that showed a higher growth temperature at ≈370 °C, the low temperature grain growth could be attributed to the precipitation and oxidation of the metal, as shown in following reactions[27]

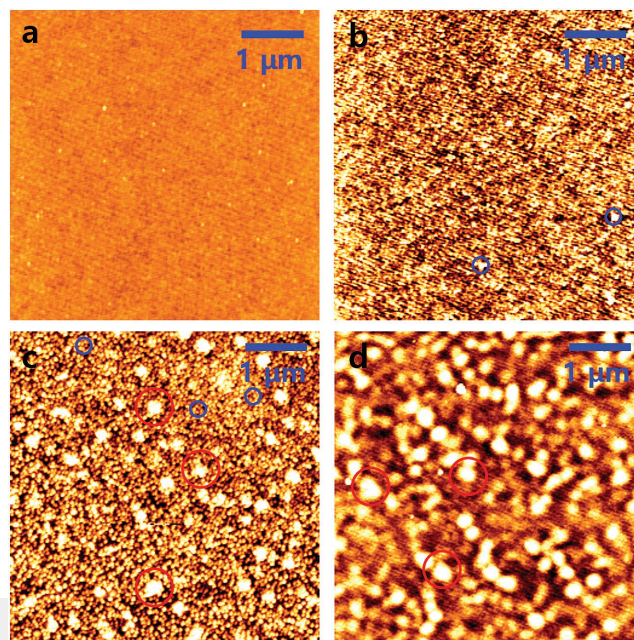

Figure 3. Atomic force microscopy (AFM) images of the $In_7Zn_3O_{13.5-\delta}$ films after H_2 reduction process at postannealing temperature of a) 250 °C, b) 300 °C, c) 350 °C, and d) 400 °C.

$$O_o^x + H_2(g) \rightarrow V_o + 2e^- + H_2O(g) \quad (1)$$

$$In^{3+} + 3e^- \rightarrow In(s) \quad (2)$$

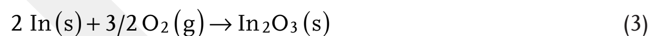

$$2\ In(s) + 3/2\ O_2(g) \rightarrow In_2O_3(s) \quad (3)$$

It is worth noting that the amorphous phase is the thermodynamically more unstable and activated state compared to the corresponding crystalline state. Thus, the increase in reactivity and decrease in on-set temperature of reduction can be attributed to the weak lattice structure of amorphous phase materials.[28]

Since increasing the reduction temperature above 450 °C caused significant morphological degradation of the a-$In_7Zn_3O_{13.5}$ films, their AFM images could not be obtained. Therefore, we analyzed the a-IZO films that were reduced at 450 and 500 °C by using a field emission scanning electron microscope and energy dispersive X-ray (EDX) spectroscopy (**Figure 4**). It was found that the higher temperature reduction of a-$In_7Zn_3O_{13.5}$ films resulted in indium metal precipitation and oxidation. While the relatively low RMS roughness of a few nanometers was calculated for the IZO films after H_2 postannealing up to 400 °C, the growth of micrometer-sized In_2O_3 nanorods from amorphous films could easily be observed (Figure 4a) at higher temperature of the reduction treatment (at 450–500 °C). Furthermore, the EDX analysis of 500 °C postreduced a-$In_7Zn_3O_{13.5}$ film (Figure 4b) confirmed the indium (In)-enriched and zinc (Zn)-enriched atomic compositions of the nanorods (spot 1) and plain films (spots 2 and 3), respectively. The metal enrichment in each region indicated that In is more easily reduced from the a-$In_7Zn_3O_{13.5}$ film, and subsequently

 © 2017 WILEY-VCH Verlag GmbH & Co. KGaA, Weinheim

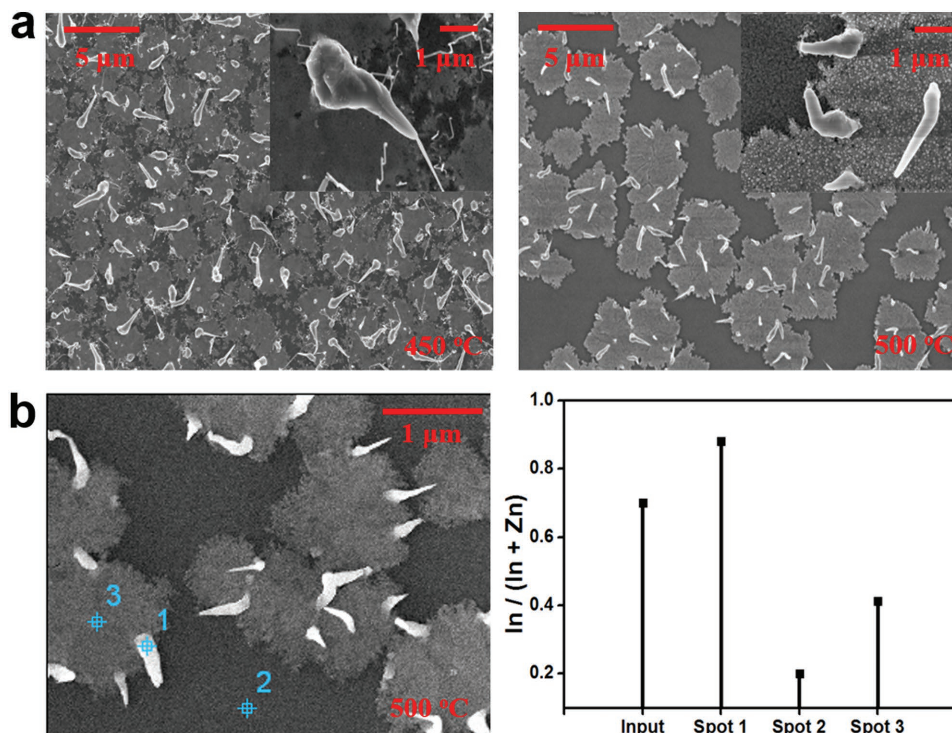

Figure 4. a) Field emission scanning electron microscopic (FE-SEM) images and b) energy dispersive X-ray (EDX) spectroscopic analysis of the $In_7Zn_3O_{13.5\text{-}\delta}$ films after H_2 postreduction at 450 and 500 °C.

forms In droplets and is reoxidized into nanorods. As previously reported, the reduction process from vacuum-deposited crystalline TCOs and the selective reduction of heavy metals such as Sn and In results in agglomerated metal clusters and subsequent growth of crystalline grains upon oxidation.[27,29,30]

Obviously, a high optical transparency is a critical requirement for high-performance TCO films. The UV–vis spectra in Figure S3 of the Supporting Information show the optical transparency of IZO films on a glass substrate with respect to different molar ratios of In and Zn after forming gas reduction treatment at 250 °C. Despite small differences in the UV–vis spectra between films of various compositions, the amorphous oxide films, particularly those of $In_7Zn_3O_{13.5}$, exhibited high optical transparency of more than 90% at wavelengths around 550 nm. These results revealed that our solution-processed and low temperature H_2-reduced TCOs are suitable for typical optoelectronic applications.[1,31]

Figure 5 shows electrical performances of the IZO films with various chemical compositions and postreduction conditions. As shown in Figure 5a,b, as-deposited a-$In_7Zn_3O_{13.5}$ film had low electrical conductivity of 4.7 S cm^{-1}, and it was not able to be characterized with Hall measurement. The highly oxidizing ambient suppressed oxygen vacancy generation, which resulted in poor electrical conductivity. Actually, the solution-processed a-$In_7Zn_3O_{13.5}$ have been implemented as a channel material in AOS TFTs with moderately low carrier concentration and high carrier mobility.[16,25] In order to activate the oxygen vacancies for generating the free carriers, the AOS films were postreduced with 5% H_2/95% Ar forming gas at various temperatures.

As shown in Figure 5a, the electrical conductivities of a-$In_7Zn_3O_{13.5}$ films progressively increased up to 250 °C. The initial conductivity of the as-deposited film (4.7 S cm^{-1}) was significantly improved to 67 S cm^{-1} after reducing the film at 150 °C, which is mostly attributed to the typical oxygen vacancy generation and subsequently increased free carrier concentration. When the annealing temperature was further increased to 250 °C, the electrical conductivity was also appreciably improved to the highest value of 298 S cm^{-1}, with a remarkably high electron mobility of 17.2 cm^2 V^{-1} s^{-1}. Interestingly, the high temperature reduction treatment of a-$In_7Zn_3O_{13.5}$ over 300 °C decreased their electrical conductivities, despite the gradual increase in carrier concentration up to 400 °C. Considering the relatively small increase in carrier concentration compared to the large increase of electron mobility, the postreduction treatment after initial vacancy generation would be more effective for filling the electrical defects than the free carrier generation. Under high temperature reduction conditions, the metal reduction and reoxidation processes induced a crystalline grain growth and disconnection of those grains, as shown in Figure 3, which resulted in a decrease in the carrier mobility and subsequent deterioration of the electrical conductivity. Note that the reducing treatment of a-$In_7Zn_3O_{13.5}$ films above 450 °C resulted in completely insulated films due to poor film morphology, as shown in Figure 4 (See **Table 1** for summarized data). The optimized activation temperature was determined to be 250 °C and therefore, the electrical conductivities of the solution-processed amorphous $In_{11\text{-}2x}Zn_{2x\text{-}1}O_{15.5\text{-}x}$ films were investigated with various metal element ratios ($x = 1$–5) under the same conditions. As **Table 2** shows, although

© 2017 WILEY-VCH Verlag GmbH & Co. KGaA, Weinheim

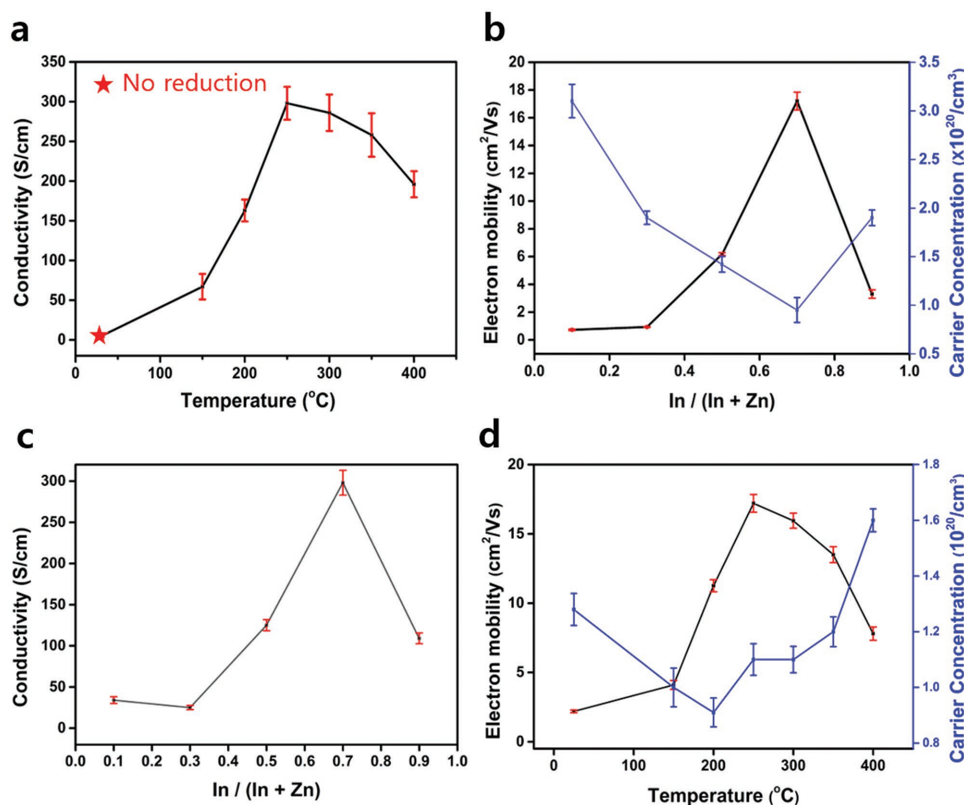

Figure 5. Electrical performance of IZO-based TCO films. a) Electrical conductivity of IZO films dependent on H_2 reduction temperature, b) correlation between electron mobility and carrier concentration of amorphous $In_7Zn_3O_{13.5-\delta}$ films dependent on H_2 reduction temperature, c) conductivity of the IZO films after H_2 reduction at 250 °C with respect to In:Zn ratio, d) correlation between the electron mobility and the carrier concentration of the IZO films after H_2 reduction at 250 °C with respect to the In:Zn ratio.

the free electron concentration was lower for this composition in comparison to the others, generally higher electrical conductivities were obtained from the amorphous IZO films with higher carrier mobility. As mentioned earlier, the poor film morphology of the Zn-rich region is consistent with the poor electron mobility values of both $In_1Zn_9O_{10.5}$ and $In_3Zn_7O_{11.5}$. In comparison to the high indium content $In_9Zn_1O_{14.5}$ film, *a*-$In_7Zn_3O_{13.5}$ still showed the highest electron mobility up to 17.2 cm^2 V^{-1} s^{-1}. Notably, as reported for the AOSs TFTs, the incorporation of Zn into the *a*-IZO film typically resulted in structural relaxation and mobility increase, usually with optimized values around In:Zn = 7:3.[16,25,32,33]

Figure 6 shows the X-ray photoelectron spectroscopy (XPS) spectra of *a*-$In_7Zn_3O_{13.5}$ with various reducing temperatures from 150 to 350 °C. The O1*s* XPS spectra of *a*-$In_7Zn_3O_{13.5}$ in Figure 6a can be deconvoluted into three peaks: (1) M–O–M lattice species at 529.6 eV, (2) oxygen in oxide lattices with oxygen vacancies (V_o) at 530.7 eV, and (3) oxygen in hydroxyl groups (M–OH) at 531.8 eV. The whole spectrum of *a*-$In_7Zn_3O_{13.5}$ in Figure 6b confirmed the existence of In, Zn, and O species. Based on the peaks assigned to M–O–M lattice and oxygen species with oxygen vacancies, the relative ratio of oxygen peaks in M–O–M lattice with respect to oxygen vacancies (V_o) peaks are represented in Figure 6c.

Interestingly, the relative ratio trend across H_2 reduction temperature was well consistent with the carrier concentration change. The H_2 postreduction treatment has known that it would be an efficient way to generate oxygen vacancies with the mechanism shown below[17,29,34]

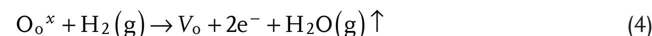

$$O_o{}^x + H_2(g) \rightarrow V_o + 2e^- + H_2O(g)\uparrow \quad (4)$$

Considering the large conductivity increase from 4.7 S cm^{-1} of the as-deposited *a*-IZO to 67 S cm^{-1} of the *a*-IZO reduced at 150 °C, it was contradictory that there was a slight increase in

Table 1. Electrical parameters of the $In_7Zn_3O_{13.5-\delta}$ films dependent on H_2 reduction temperature from 150 to 400 °C in addition to an as-deposited film.

Parameters	$In_7Zn_3O_{13.5-\delta}$						
	As-deposited	150 °C	200 °C	250 °C	300 °C	350 °C	400 °C
Conductivity, σ [S cm^{-1}]	4.7	67.0	163.0	298.0	286.0	258.0	196.0
Mobility, μ [cm^2 V^{-1} s^{-1}]	NA	4.10	11.3	17.2	16.0	13.5	7.80
Carrier density, n (x 10^{20}) [cm^{-3}]	NA	1.0	0.9	1.1	1.1	1.2	1.6

© 2017 WILEY-VCH Verlag GmbH & Co. KGaA, Weinheim

Table 2. Electrical parameters of the IZO films with respect to In:Zn ratio dependent after H_2 reduction at 250 °C.

Parameters	H_2 reduction at 250 °C				
	$In_1Zn_9O_{10.5-\delta}$	$In_3Zn_7O_{12.5-\delta}$	$In_5Zn_5O_{13.5-\delta}$	$In_7Zn_3O_{13.5-\delta}$	$In_9Zn_1O_{14.5-\delta}$
Conductivity, σ [S cm^{-1}]	34.0	25.0	125.0	298.0	109.0
Electron Mobility, μ [cm^2 V^{-1} s^{-1}]	0.73	0.93	6.17	17.2	3.30
Carrier Density, n [x 10^{20} cm^{-3}]	2.9	1.7	1.3	1.1	2.1

oxygen vacancy concentration between the IZO films with no posttreatment and after H_2 reduction at 150 °C, as shown in Figure 6b. It can be postulated that an abundance of oxygen vacancy sites was intrinsically generated during film formation, and replaced by hydrogen species in form of H_o^-.[33] The pristine *a*-IZO films with In-rich composition consisted of various amounts of oxygen vacancies, most of which were occupied as deep trap states in the electronic structure of the *a*-IZO films.[35,36] Facile generation of the oxygen vacancies in In-rich oxide films has been typically reported in studies related to electrical and optical instability generated via negative bias illumination stress test, both in *a*-IZO and *a*-IGZO-based TFTs.[20,35,37] Especially, more than 99% of the oxygen vacancies in the *a*-IZO films generated deep-level defects in the mid-gap

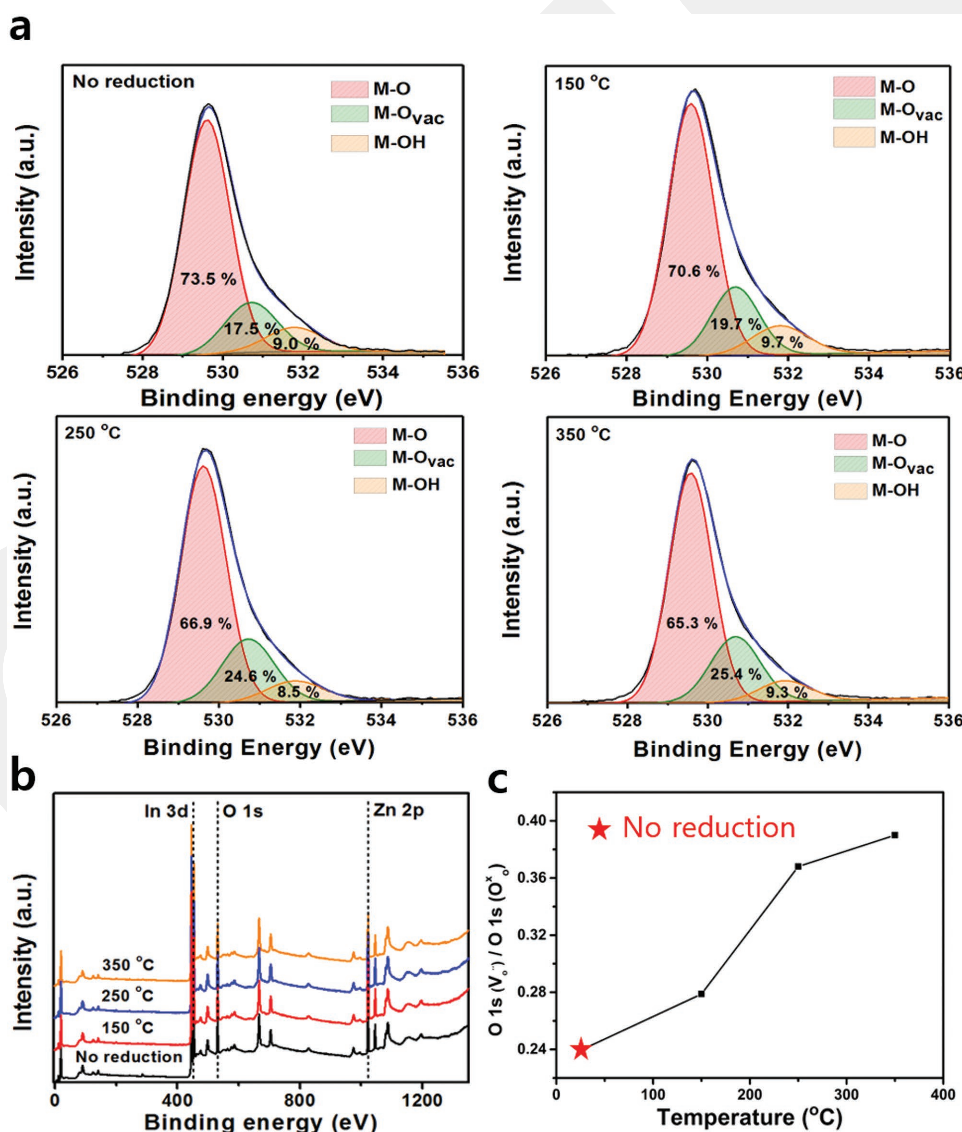

Figure 6. a) O 1s X-ray photoelectron spectra (XPS) of the $In_7Zn_3O_{13.5-\delta}$ films with as-deposited and after H_2 postreduction from 150 to 350 °C, b) their atomic scans and c) the relative concentrations of oxygen vacancies in the $In_7Zn_3O_{13.5-\delta}$ films. All calculations were performed based on an area integration of each O 1s peak. O1s (O^x_o) and O1s ($V_o^{··}$) denote the O1s features due to oxide lattices without oxygen vacancies and with oxygen vacancies, respectively.

 © 2017 WILEY-VCH Verlag GmbH & Co. KGaA, Weinheim

states, rather than shallow localized states beneath the conduction band minimum.[35,36] The postreduction treatment in mild temperature ranges (T_{red} ≈ 150–400 °C) is more closely related to the lattice relaxation rather than carrier generation. With a mild postreduction, a number of localized spots that were related to distorted lattices could be structurally relieved as the electrons would be supported by the H_o^- filled deep trap states.[33] Therefore, this structural lattice relaxation resulted in mobility enhancement, which was derived mainly from the low effective mass of the electrons and better dispersive overlap of the In 5s orbital in IZO films.[33] Overall, the rapid increase in electron mobility up to 250 °C and the moderate increase in carrier concentration are well-matched with the role of the hydrogen molecule.[33] It is worth noting that the suppression of electron mobility at a high annealing temperature of more than 250 °C is closely related to reduction of the metal and subsequent film aggregation, which resulted in severe degradation of electrical performance as the electron transporting pathways break down. The electrical stability in Figure S5 of the Supporting Information shows relative resistivity change ratio (ρ/ρ_0) of 3.13 and 9.76 after 105 h storage at room temperature and 70 °C, respectively. With the high temperature storage, the O_2 and H_2O from ambient atmosphere could remove the H_o^- and oxygen vacancy and degrade the electrical performance.[38] The oxidation fragile TCO performance could be enhanced with thickness optimization and film quality improvement.[39]

In order to confirm the requirements for mild postreduction treatment of AOS-based TCO films without mobility degradation, other AOS materials such as *a*-ZTO ($Zn_{0.3}Sn_{0.7}O_{1.7}$) and *a*-ZITO ($Zn_{0.7}In_{0.6}Sn_{0.7}O_{3.0}$) were also characterized. These materials were spin-casted from the precursor solution and subsequently annealed at 400 and 500 °C under ambient air. Similar to the *a*-IZO film, postreduction around 250–300 °C gave the highest conductivities of 23.4 S cm^{-1} (at 250 °C) and 59.0 S cm^{-1} (at 300 °C) for *a*-ZTO and *a*-ZITO, respectively. As shown in Table S2 of the Supporting Information, the high temperature reduction over 350 °C of both *a*-ZTO and *a*-ZITO films also resulted in their severe degradation, which affected their electrical conductivity values. As shown in Figure S1 of the Supporting Information, the Sn containing amorphous oxide films lack clear crystalline GIAXRD peak evolutions even after high temperature reduction treatment at 350 and 450 °C for *a*-ZTO and *a*-ZITO films, respectively. The broad poorly crystalline SnO_2 peaks were observed for 450 °C reduced *a*-ZTO films. In Sn containing AOSs, such as *a*-ZTO and *a*-ZITO, the Sn also can be reduced with subsequent formation of SnO_x.[27,29] Since the amorphous SnO_x have been reported with significantly higher $T_{crystallization}$ ≈ 450–550 °C than $T_{crystallization}$ ≈ 180 °C of amorphous InO_x, the reduced oxide films could remain as amorphous phase.[40] In addition, the multinary oxides formation with simultaneously reduced In and Sn could result amorphous In–Sn–O (*a*-ITO) with high crystallization temperature.[41] Overall, the postreduction of *a*-ZITO and *a*-ZTO films did not show clear crystalline peaks due to high crystallization temperatures of *a*-SnO_x and *a*-ITO. However, similar to the grain segregation behavior of high temperature reduced *a*-IZO films, the AFM images of *a*-ZITO in Figure S4 of the Supporting Information show that high temperature reduction of *a*-ZITO also induced significant metal dissolution from amorphous matrix and subsequent disconnected domains.

The solution-processed *a*-$In_7Zn_3O_{13.5}$ TCO films were employed as an anode in bulk-heterojunction organic photovoltaic (BHJ-OPV) cells. **Figure 7**a shows a typical structure of the

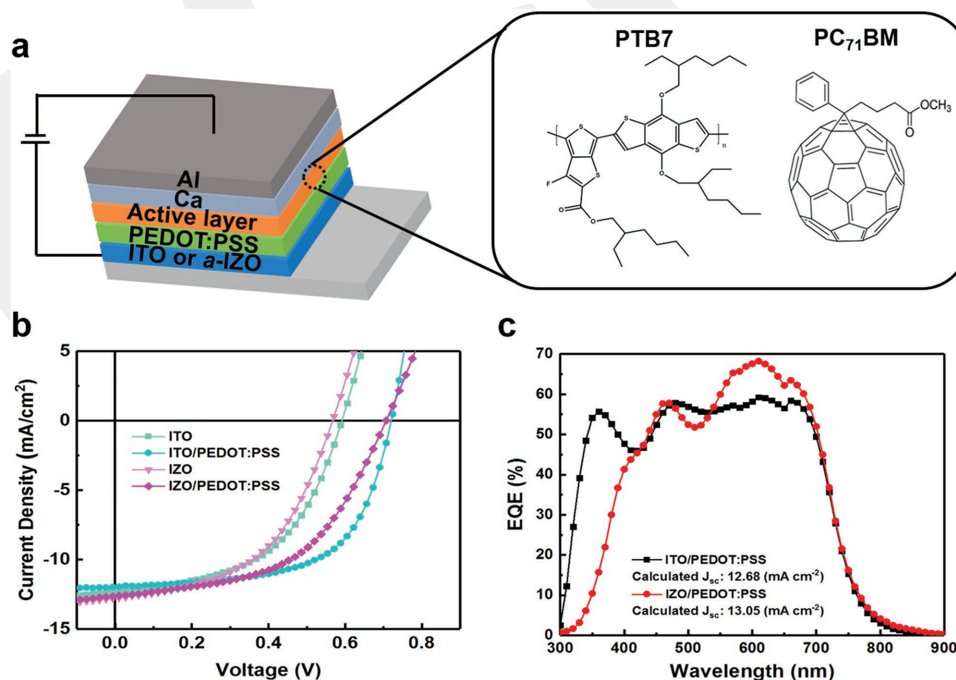

Figure 7. Photovoltaic characteristics of organic solar cell based on ITO or IZO transparent anodes. a) Schematic device architecture and chemical structures of donor polymer (PTB7) and acceptor molecule ($PC_{71}BM$), b) *J*–*V* plots and c) EQE spectra of the OPVs with two different electrodes.

© 2017 WILEY-VCH Verlag GmbH & Co. KGaA, Weinheim

OPV devices. The photoactive layer was composed of poly[[4,8-bis[(2-ethylhexyl)oxy]benzo[1,2-*b*:4,5-*b*′]dithiophene-2,6-diyl][3-fluoro-2-[(2-ethylhexyl)carbonyl]thieno[3,4-*b*]thiophenediyl]] and [6,6]-phenyl-C_{71}-butyric acid methyl ester (PTB7:$PC_{71}BM$), and was fabricated with the PEDOT:PSS interfacial layer together with the Ca/Al cathode electrode. As shown in Figure 7b,c, the current density versus voltage (*J*–*V*) characteristics and external quantum efficiencies (EQEs) of the *a*-IZO-based OPV devices were compared with those of the ITO-based reference devices. The ITO/PEDOT:PSS devices exhibited a power conversion efficiency (PCE) of 5.3% with an open-circuit voltage (V_{OC}) of 0.72 V, a short-circuit current (J_{SC}) of 11.9 mA cm^{-2}, and a fill factor (FF) of 61.5. Meanwhile, the *a*-IZO/PEDOT:PSS devices presented a similar PCE of 4.6% with $V_{OC} = 0.71$ V, $J_{SC} = 12.6$ mA cm^{-2}, and FF = 51.7. Notably, the quantum efficiency of our *a*-IZO-based OPV device was higher than that of the ITO device at wavelengths of ≈650 nm, while the quantum efficiencies differed in the short wavelength region (below 400 nm). This can be attributed to the higher transmittance of the *a*-IZO electrode at ≈650 nm and a lower transmittance at shorter wavelengths in comparison to the transmittance of the ITO electrode. These EQE results are also consistent with the slightly higher J_{SC} values observed for the *a*-IZO device. As shown above, the main reason for the slightly lower performance of the *a*-IZO devices is attributed to the decreased FF rather than the V_{OC} and J_{SC} values because of the lower conductivity of *a*-IZO (298 S cm^{-1}) and larger sheet resistance than those of ITO-based reference OPVs. Thus, it is expected that the efficiency of the OPVs can be further improved if a more optimized fabrication process involving thicker films is introduced for the purpose of resolving the low conductivity issues of low-cost solution-processed AOS TCOs films. These results reveal that the mild reduction treatment of AOSs in the H_2 environment developed in this work can be employed as a general methodology for obtaining printed and flexible TCO films with high electrical performance for applications in a number of large-area optoelectronic devices.

3. Conclusion

In this work, we investigated the optimized activation route for developing solution-processed amorphous IZO films via postreduction treatment under 5% hydrogen forming gas condition. Because of the vulnerable metal reduction method, typical solution-based AOS TCOs suffer from severe degradation of film morphology and subsequent electrical performance deterioration. The mild temperature reduction treatment of *a*-IZO around 250 °C enabled us to achieve an optimal activation of the TCO films with the highest electrical conductivity of 298 S cm^{-1} and electron mobility of 17.2 cm^2 V^{-1} s^{-1}, which is unprecedented via solution-process. Unlike the crystalline materials, the reduction treatment with hydrogen induced a large free carrier concentration with oxygen vacancy generation and also led to the passivation of defects by inducing a structural relaxation of the M–O–M lattice by filling of the deep-trap states, which occupy most of the mid-states in the *a*-IZO band structure. Furthermore, a similar mild temperature activation of various solution-processed AOS-based TCOs such as *a*-ZTO and *a*-ZITO also confirmed the importance of postreduction conditions. For AOS-based TCO fabrication, the synergetic implementation of optimized AOS activation methodology and low-temperature AOS film synthesis methods, such as combustion method, photochemical activation, and "sol–gel on chip" process, would further lower the processing temperature and enhance electric performance of solution-processed thin film materials.[12,13,25] Finally, we have demonstrated the high electrical performance of TCO films for printable, large-area optoelectronic applications. In comparison to the ITO reference device, PTB7:$PC_{71}BM$-based OPV cells incorporating the optimized *a*-IZO TCOs showed similar OPV characteristics. Considering the mild optimization temperature, the solution-processed AOS-based TCOs could be further applied to low-budget thermally flexible substrates.

4. Experimental Section

Preparation of Solution Precursors: Indium nitrate hydrate ($In(NO_3)_3{\cdot}xH_2O$, 99%), zinc nitrate hexahydrate (98%), zinc acetate dihydrate (99%), indium(III) chloride (98%), tin(IV) chloride pentahydrate (98%), ethanolamine (99.5%), ammonium nitrate (98%), and 2-methoxyethanol (anhydrous, 99.8%) were purchased from Sigma-Aldrich. All reagents were used as-received without further purification. The In and Zn precursor solutions were prepared by dissolving 3.776 g $In(NO_3)_3{\cdot}xH_2O$ ($x \approx 4.25$) or 2.975 g $Zn(NO_3)_2{\cdot}6H_2O$ in 25 mL 2-methoxyethanol, respectively. After complete dissolution of the metal salts, the mixed solutions were aged at 70 °C overnight. For the 10 mL IZO precursor solution, the In and Zn solutions were mixed to achieve In/(In + Zn) = 10%, 30%, 50%, 70%, 90% mol mol^{-1} ratio, the solutions were stirred at room temperature overnight. 0.4 M zinc–indium–tin oxide (ZITO, Zn:In:Sn = 0.35:0.3:0.35) precursor solutions were prepared by dissolving 307.3 mg $Zn(Ac)_2{\cdot}2H_2O$, 265.4 mg $InCl_3$, 490.8 mg $SnCl_4{\cdot}5H_2O$, and 120 µL ethanolamine in 10 mL 2-methoxyethanol. In case of 0.4 M zinc–tin oxide (ZTO, Zn:Sn = 3:7) precursor solutions, the mixture was prepared by 356.88 mg $Zn(NO_3)_2{\cdot}6H_2O$, 530.94 mg $SnCl_2$, and 224.11mg NH_4NO_3 in 10 mL 2-methoxyethanol.

Film Deposition and Transparent Conductive Electrode Fabrication: The 0.4 M of metal ion concentration *a*-IZO precursor solution was spin-coated at 3500 rpm for 30 s onto SiO_2 substrates or glasses, and the spin-coated samples were then annealed at 500 °C for 20 min under air ambient condition. The IZO films were overcoated at the same speed for desired thickness, and annealed for 20 min under the same ambient condition. The postreduction annealing of the IZO samples was carried out in forming gas (5% H_2 and 95% Ar)-filled tube furnace for 1 h up to desired temperature. For characterizing the IZO transparent conductive films, the samples were patterned by placing antistick 3 M 5480 polytetrafluoroethylene tape on top of the conductive oxide films. The unprotected areas were etched by dipping the film into 12 M HCl for 1 min, and the remained residues were removed using iso-propanol sonication, followed by hexane sonication. Indium metal was deposited for suitable contact.

Characterization of IZO Film: Grazing incident X-ray diffraction scans were obtained using X'pert Pro (PANalytical, The Netherlands) using Cu Kα radiation. The atomic force microscopy images with noncontact mode were obtained with XE-120-AFM (Park Systems, Korea). Al-coated noncontact tips (Nanosensors, PPP-NCHR, Switzerland, force constant (k) = 42 N m^{-1}, resonance frequency = 330 kHz) were used for the atomic force microscopy imaging, and the scan rate was 0.5 Hz and the scan size was 5 µm × 5 µm. The sheet resistance was measured with the probe station (MST-4000A, MS TECH) using the Van der Pauw configuration. Carrier mobility and carrier concentration of the IZO films were performed with a Hall measurement system (magnetic force: 0.559 T, current: 10 mA). The electrical stability tests were performed at room temperature (25–30 °C) and 70 °C and relative humidity level of 20%.

© 2017 WILEY-VCH Verlag GmbH & Co. KGaA, Weinheim

Organic Photovoltaic Devices Fabrication and Characterization: The a-$In_7Zn_3O_{13.5-\delta}$ (a-IZO) TCO film was prepared by the same procedure mentioned above. In brief, a-IZO was spin-coated on 1.5 cm × 1.5 cm glass substrates at 3500 rpm and followed by H_2-reduction at 250 °C for 1 h. The a-IZO film was patterned with 12 M HCl for 1 min. For a BHJ photoactive solution, PTB7 (1-material) and $PC_{71}BM$ (Nano-C) were dissolved in a mixture of chlorobenzene (95 vol%)/1,8-diiodooctance (5 vol%) with a polymer:fullerene weight ratio of 1:1.5 and stirred 60 °C overnight. The concentration was 10 mg mL^{-1} with respect to the polymer. While ITO-covered glass substrates for reference device were cleaned by ultrasonication in acetone and iso-propanol for 10 min each and exposed to UV/O_3 for 20 min, there was no cleaning step in case of the IZO/glass substrates. As an anode interfacial layer, PEDOT:PSS (Clevios P VP Al 4083, Heraeus) was spin-coated with 5000 rpm for 40 s onto the ITO/glass substrates and annealed at 150 °C for 10 min under ambient condition. However, only natural drying without thermal baking was conducted in case of IZO/glass substrates after PEDOT:PSS deposition. The PTB7:$PC_{71}BM$ active layer was deposited by spin-coating the BHJ solution at 2000 rpm for 40 s, and then 20 nm of Ca and 100 nm of Al were deposited through a metal shadow mask (the device active area: 4.64 mm^2) by thermal evaporation under high-vacuum condition ($\approx 1.0 \times 10^{-6}$ Torr). The current density versus voltage (J–V) curves were measured through a Keithley 2400 instrument under 100 mW cm^{-2} illumination with AM 1.5G simulating condition. The light intensity was calibrated with an NREL-calibrated KG5 filtered silicon reference cell. The EQE spectra were measured via a Quantum Efficiency Measurement System (IQE-200, Oriel).

Supporting Information

Supporting Information is available from the Wiley Online Library or from the author.

Acknowledgements

B.D.C., J.P., and K.-J.B. contributed equally to this work. This work was supported in part by the National Research Foundation of Korea (NRF) grant funded by the Korea government (MSIP) (Nos. NRF-2016K2A9A1A06924256 and NRF-2017R1C1B2005254) and the Technology Innovation Program (No. 10065651) funded by MOTIE/KEIT.

Conflict of Interest

The authors declare no conflict of interest.

Keywords

activation treatments, amorphous oxide semiconductors, indium–zinc oxide, oxide solution-processing, transparent conductive electrodes

Received: August 16, 2017
Revised: November 6, 2017
Published online:

[1] K. Ellmer, *Nat. Photonics* **2012**, *6*, 809.
[2] H. Hosono, D. C. Paine, D. Ginley, *Handbook of Transparent Conductors*, Springer Science & Business Media, New York, NY **2010**.
[3] a) Y. Yang, Q. Huang, A. W. Metz, J. Ni, S. Jin, T. J. Marks, M. E. Madsen, A. DiVenere, S. T. Ho, *Adv. Mater.* **2004**, *16*, 321; b) S. Laux, N. Kaiser, A. Zöller, R. Götzelmann, H. Lauth, H. Bernitzki, *Thin Solid Films* **1998**, *335*, 1; c) S. Ishibashi, Y. Higuchi, Y. Ota, K. Nakamura, *J. Vac. Sci. Technol., A* **1990**, *8*, 1403; d) H. Kim, J. Horwitz, G. Kushto, Z. Kafafi, D. Chrisey, *Appl. Phys. Lett.* **2001**, *79*, 284.
[4] A. Facchetti, T. Marks, *Transparent Electronics: From Synthesis to Applications*, John Wiley & Sons, Chichester, UK **2010**.
[5] a) T. Minami, H. Nanto, S. Takata, *Jpn. J. Appl. Phys.* **1984**, *23*, L280; b) B. Stjerna, E. Olsson, C. Granqvist, *J. Appl. Phys.* **1994**, *76*, 3797; c) H. Lee, S. Lau, Y. Wang, K. Tse, H. Hng, B. Tay, *J. Cryst. Growth* **2004**, *268*, 596; d) S. R. Taylor, S. M. McLennan, *Rev. Geophys.* **1995**, *33*, 241.
[6] a) J. Burschka, N. Pellet, S.-J. Moon, R. Humphry-Baker, P. Gao, M. K. Nazeeruddin, M. Grätzel, *Nature* **2013**, *499*, 316; b) P. D. Batista, M. Mulato, *J. Mater. Sci.* **2010**, *45*, 5478; c) F. Hao, C. C. Stoumpos, D. H. Cao, R. P. Chang, M. G. Kanatzidis, *Nat. Photonics* **2014**, *8*, 489; d) T. Stubhan, H. Oh, L. Pinna, J. Krantz, I. Litzov, C. J. Brabec, *Org. Electron.* **2011**, *12*, 1539.
[7] a) M. A. Meyers, A. Mishra, D. J. Benson, *Prog. Mater. Sci.* **2006**, *51*, 427; b) C. Peng, Z. Jia, D. Bianculli, T. Li, J. Lou, *J. Appl. Phys.* **2011**, *109*, 103530; c) S. K. Park, J. I. Han, D. G. Moon, W. K. Kim, *Jpn. J. Appl. Phys.* **2003**, *42*, 623; d) Z. Chen, B. Cotterell, W. Wang, E. Guenther, S.-J. Chua, *Thin Solid Films* **2001**, *394*, 201.
[8] a) L. Petti, N. Münzenrieder, C. Vogt, H. Faber, L. Büthe, G. Cantarella, F. Bottacchi, T. D. Anthopoulos, G. Tröster, *Appl. Phys. Rev.* **2016**, *3*, 021303; b) J. Song, H. Zeng, *Angew. Chem., Int. Ed.* **2015**, *54*, 9760.
[9] D. S. Hecht, L. Hu, G. Irvin, *Adv. Mater.* **2011**, *23*, 1482.
[10] a) P. Solís-Fernández, M. Bissett, H. Ago, *Chem. Soc. Rev.* **2017**, *46*, 4572; b) M. Cann, M. J. Large, S. J. Henley, D. Milne, T. Sato, H. Chan, I. Jurewicz, A. B. Dalton, *Mater. Today Commun.* **2016**, *7*, 42; c) K. S. Novoselov, V. Fal, L. Colombo, P. Gellert, M. Schwab, K. Kim, *Nature* **2012**, *490*, 192; d) A. Chortos, J. Liu, Z. Bao, *Nat. Mater.* **2016**, *15*, 937.
[11] a) D. Kim, B. Hwang, J. Park, H. Jeon, B. Bae, H. Lee, N.-E. Lee, *Org. Electron.* **2012**, *13*, 2401; b) J. Sheng, H.-J. Lee, S. Oh, J.-S. Park, *ACS Appl. Mater. Interfaces* **2016**, *8*, 33821; c) J.-S. Park, T.-W. Kim, D. Stryakhilev, J.-S. Lee, S.-G. An, Y.-S. Pyo, D.-B. Lee, Y. G. Mo, D.-U. Jin, H. K. Chung, *Appl. Phys. Lett.* **2009**, *95*, 013503.
[12] a) S. R. Thomas, P. Pattanasattayavong, T. D. Anthopoulos, *Chem. Soc. Rev.* **2013**, *42*, 6910; b) B. Du Ahn, H.-J. Jeon, J. Sheng, J. Park, J.-S. Park, *Semi. Sci. Technol.* **2015**, *30*, 064001; c) Y. S. Rim, H. Chen, Y. Liu, S.-H. Bae, H. J. Kim, Y. Yang, *ACS Nano* **2014**, *8*, 9680; d) Y.-H. Kim, J.-S. Heo, T.-H. Kim, S. Park, M.-H. Yoon, J. Kim, M. S. Oh, G.-R. Yi, Y.-Y. Noh, S. K. Park, *Nature* **2012**, *489*, 128; e) J. Liu, D. B. Buchholz, R. P. Chang, A. Facchetti, T. J. Marks, *Adv. Mater.* **2010**, *22*, 2333.
[13] M.-G. Kim, M. G. Kanatzidis, A. Facchetti, T. J. Marks, *Nat. Mater.* **2011**, *10*, 382.
[14] a) Z. Chen, W. Li, R. Li, Y. Zhang, G. Xu, H. Cheng, *Langmuir* **2013**, *29*, 13836; b) A. Banerjee, S. Kundoo, P. Saha, K. Chattopadhyay, *J. Sol-Gel Sci. Technol.* **2003**, *28*, 105; c) W. Tang, D. Cameron, *Thin Solid Films* **1994**, *238*, 83; d) A. Nadarajah, M. E. Carnes, M. G. Kast, D. W. Johnson, S. W. Boettcher, *Chem. Mater.* **2013**, *25*, 4080; e) J. Song, S. A. Kulinich, J. Li, Y. Liu, H. Zeng, *Angew. Chem., Int. Ed.* **2015**, *127*, 472; f) R. M. Pasquarelli, C. J. Curtis, A. Miedaner, M. F. van Hest, R. P. O'Hayre, D. S. Ginley, *Inorg. Chem.* **2010**, *49*, 5424.
[15] M.-G. Kim, J. W. Hennek, H. S. Kim, M. G. Kanatzidis, A. Facchetti, T. J. Marks, *J. Am. Chem. Soc.* **2012**, *134*, 11583.
[16] K. Song, D. Kim, X.-S. Li, T. Jun, Y. Jeong, J. Moon, *J. Mater. Chem.* **2009**, *19*, 8881.

© 2017 WILEY-VCH Verlag GmbH & Co. KGaA, Weinheim

[17] R. M. Pasquarelli, D. S. Ginley, R. O'Hayre, *Chem. Soc. Rev.* **2011**, *40*, 5406.
[18] L. Petti, H. Faber, N. Münzenrieder, G. Cantarella, P. A. Patsalas, G. Tröster, T. D. Anthopoulos, *Appl. Phys. Lett.* **2015**, *106*, 092105.
[19] M. P. Taylor, D. W. Readey, M. F. van Hest, C. W. Teplin, J. L. Alleman, M. S. Dabney, L. M. Gedvilas, B. M. Keyes, B. To, J. D. Perkins, *Adv. Funct. Mater.* **2008**, *18*, 3169.
[20] a) P. Barquinha, G. Goncalves, L. Pereira, R. Martins, E. Fortunato, *Thin Solid Films* **2007**, *515*, 8450; b) Y. Ogo, K. Nomura, H. Yanagi, T. Kamiya, M. Hirano, H. Hosono, *Phys. Status Solidi* **2008**, *205*, 1920; c) S.-J. Seo, C. G. Choi, Y. H. Hwang, B.-S. Bae, *J. Phys. D: Appl. Phys.* **2008**, *42*, 035106; d) K. Nomura, A. Takagi, T. Kamiya, H. Ohta, M. Hirano, H. Hosono, *Jpn. J. Appl. Phys.* **2006**, *45*, 4303.
[21] J. Ko, I. Kim, D. Kim, K. Lee, T. Lee, B. Cheong, W. Kim, *Appl. Surf. Sci.* **2007**, *253*, 7398.
[22] A. J. Leenheer, J. D. Perkins, M. F. Van Hest, J. J. Berry, R. P. O'Hayre, D. S. Ginley, *Phys. Rev. B* **2008**, *77*, 115215.
[23] N. Ito, Y. Sato, P. Song, A. Kaijio, K. Inoue, Y. Shigesato, *Thin Solid Films* **2006**, *496*, 99.
[24] M. P. Taylor, D. W. Readey, C. W. Teplin, M. F. van Hest, J. L. Alleman, M. S. Dabney, L. M. Gedvilas, B. M. Keyes, B. To, J. D. Perkins, *Meas. Sci. Technol.* **2004**, *16*, 90.
[25] K. Banger, Y. Yamashita, K. Mori, R. Peterson, T. Leedham, J. Rickard, H. Sirringhaus, *Nat. Mater.* **2011**, *10*, 45.
[26] D.-J. Lee, J.-Y. Kwon, J. Kim, K.-J. Kim, Y.-H. Cho, S.-Y. Cho, S.-H. Kim, J. Xu, K.-B. Kim, *J. Phys. Chem. C* **2013**, *118*, 408.
[27] G. Guenther, G. Schierning, R. Theissmann, R. Kruk, R. Schmechel, C. Baehtz, A. Prodi-Schwab, *J. Appl. Phys.* **2008**, *104*, 034501.
[28] J. Van den Meerakker, P. Baarslag, W. Walrave, T. Vink, J. Daams, *Thin Solid Films* **1995**, *266*, 152.
[29] M. Morales-Masis, L. Ding, F. Dauzou, Q. Jeangros, A. Hessler-Wyser, S. Nicolay, C. Ballif, *APL Mater.* **2014**, *2*, 096113.
[30] M. Albrecht, R. Schewski, K. Irmscher, Z. Galazka, T. Markurt, M. Naumann, T. Schulz, R. Uecker, R. Fornari, S. Meuret, *J. Appl. Phys.* **2014**, *115*, 053504.
[31] M. Morales-Masis, S. De Wolf, R. Woods-Robinson, J. W. Ager, C. Ballif, *Adv. Electron. Mater.* **2017**, *3*, 1770021.
[32] a) K. Nomura, H. Ohta, A. Takagi, T. Kamiya, M. Hirano, H. Hosono, *Nature* **2004**, *432*, 488; b) T. Kamiya, K. Nomura, H. Hosono, *Sci. Technol. Adv. Mater.* **2010**, *11*, 044305; c) H. Kumomi, S. Yaginuma, H. Omura, A. Goyal, A. Sato, M. Watanabe, M. Shimada, N. Kaji, K. Takahashi, M. Ofuji, *J. Disp. Technol.* **2009**, *5*, 531.
[33] Y. Kang, B. D. Ahn, J. H. Song, Y. G. Mo, H. H. Nahm, S. Han, J. K. Jeong, *Adv. Electron. Mater.* **2015**, *1*, 1400006.
[34] G. B. Taylor, H. W. Starkweather, *J. Am. Chem. Soc.* **1930**, *52*, 2314.
[35] S. Y. Park, J. H. Song, C.-K. Lee, B. G. Son, C.-K. Lee, H. J. Kim, R. Choi, Y. J. Choi, U. K. Kim, C. S. Hwang, *IEEE Electron Device Lett.* **2013**, *34*, 894.
[36] H.-K. Noh, K. Chang, B. Ryu, W.-J. Lee, *Phys. Rev. B* **2011**, *84*, 115205.
[37] a) S. Oh, B. Seob Yang, Y. Jang Kim, M. Sook Oh, M. Jang, H. Yang, J. Kyeong Jeong, C. Seong Hwang, H. Joon Kim, *Appl. Phys. Lett.* **2012**, *101*, 092107; b) K. Nomura, T. Kamiya, H. Hosono, *Appl. Phys. Lett.* **2011**, *99*, 053505; c) K. Nomura, T. Kamiya, H. Hosono, *J. Soc. Inf. Disp.* **2010**, *18*, 789.
[38] B. Yaglioglu, Y.-J. Huang, H.-Y. Yeom, D. C. Paine, *Thin Solid Films* **2006**, *496*, 89.
[39] T. Minami, *Thin Solid Films* **2008**, *516*, 1314.
[40] a) T. Kobayashi, Y. Kimura, H. Suzuki, T. Sato, T. Tanigaki, Y. Saito, C. Kaito, *J. Cryst. Growth* **2002**, *243*, 143; b) H. Morikawa, M. Fujita, *Thin Solid Films* **2000**, *359*, 61.
[41] M.-G. Kim, H. S. Kim, Y.-G. Ha, J. He, M. G. Kanatzidis, A. Facchetti, T. J. Marks, *J. Am. Chem. Soc.* **2010**, *132*, 10352.

© 2017 WILEY-VCH Verlag GmbH & Co. KGaA, Weinheim